

Engineering topological band conduction into KTaO_3 's two-dimensional electron gases

Zhi Gang Cheng (✉ zgcheng@iphy.ac.cn)

Institute of Physics, Chinese Academy of Sciences <https://orcid.org/0000-0002-9449-6734>

Yuting Zou

Institute of Physics, Chinese Academy of Sciences

Hyunki Shin

Quantum Matter Institute, University of British Columbia <https://orcid.org/0000-0001-8435-4479>

Haoran Wei

Institute of Physics, Chinese Academy of Sciences

Bruce Davidson

Quantum Matter Institute, University of British Columbia

Ke Zou

University of British Columbia <https://orcid.org/0000-0002-1181-1779>

Article

Keywords:

Posted Date: May 17th, 2022

DOI: <https://doi.org/10.21203/rs.3.rs-1579411/v1>

License:  This work is licensed under a Creative Commons Attribution 4.0 International License. [Read Full License](#)

Version of Record: A version of this preprint was published at npj Quantum Materials on December 29th, 2022. See the published version at <https://doi.org/10.1038/s41535-022-00536-5>.

Abstract

Two-dimensional electron gas (2DEG) systems generated at oxide interfaces that exhibit novel physics phenomena have opened up a new era for oxide-based electronics, photonics, and spintronics. The recent discovery of superconductivity plus the strong spin-orbital coupling naturally existing in the 2DEGs of KTaO_3 (KTO) makes KTO an exciting platform for the interplay of the electronic and spin degree of freedom to create new physical properties. By directly placing KTO's 2DEGs next to another strongly-correlated oxide with nontrivial topological nodes, we reveal direct evidence of topological states in the electronic transport properties of the KTO's 2DEGs, due to the electronic reconstruction caused by the proximity effect. This adds potential for new functionality in KTO heterostructures.

Introduction

Intensive attention has recently been focused on perovskite oxide heterostructures for two-dimensional electron gases (2DEGS) hosted at interfaces. A rich variety of exotic phenomena has been observed, such as metal-insulator transitions (MIT), magnetic correlations, strong tunability by an electric field, and superconductivity. A typical example is $\text{LaAlO}_3/\text{SrTiO}_3$ (LAO/STO), within which 2DEGs are formed in STO close to the interface by charge transfer due to discontinuity of polarity. It simultaneously exhibits extremely high mobility ($10,000 \text{ cm}^2\text{V}^{-1}\text{s}^{-1}$), superconductivity, ferromagnetism, and a rich electronic phase diagram¹⁻⁷. Especially, the coexistence of ferromagnetism and superconductivity makes LAO/STO an intriguing candidate for unconventional superconductivity. In addition, Rashba-type spin-orbit coupling associated with broken spatial inversion symmetry provides a convenient and promising way to manipulate magnetic structure electrically, making LAO/STO an ideal platform for practice in spintronics⁸.

With respect to STO, KTaO_3 (KTO) shares similarities but also distinct features in the crystal structure, transport properties, and band structure⁹⁻¹¹. KTO-based heterostructures accordingly host 2DEGs when oxygen vacancies are generated in KTO. Some in this series exhibit high mobility, strong spin polarization, and the recently discovered nonconventional superconductivity, etc¹²⁻¹⁸. In particular, with STO-based counterparts for which Ti $3d$ orbitals make the main contribution, KTO-based heterostructures incorporate itinerant electrons from Ta $5d$ -orbitals. Stronger spin-orbit coupling (SOC) is thus expected to introduce non-zero Berry curvature to the reciprocal space¹⁹. Topological band structures and other phenomena such as Rashba splitting may occur consequently. It has been also pointed out by recent theoretical study that topological superconductivity may be induced by in-plane magnetic field to a two-dimensional metallic system with spin-orbit couplings because spin-orbit coupling creates topologically nontrivial spin textures and could also serve as attractive force for electron pairings²⁰.

Non-trivial topology, together with existing exotic properties including superconductivity and spin polarization, enrich KTO-based heterostructure with great prospects in both fundamental research and practical applications. For instance, topological superconductivity is theoretically proven to be able to host Majorana zero modes – an essential prerequisite to realizing non-Abelian statistics – and potentially plays a key role in developing topological quantum computation¹⁵⁻¹⁸. Moreover, the strong SOC can also be used in developing novel spintronic devices such as spin-orbit torque-based magneto-resistive randomized access memory (SOT-MRAM), making KTO-based heterostructure a better candidate in spintronics compared with its STO-based counterpart.

It has been reported previously that the heterostructure of $\text{LaTiO}_3/\text{KTaO}_3$ (LTO/KTO) can host two-dimensional electron gas (2DEG) with high mobility¹⁴. In comparison with LTO, EuTiO_3 (ETO) has distinctive magnetic properties due to the partially-filled $4f$ orbitals of Eu and their exchange interaction between Ti- $3d$ and Eu- $5d$ orbitals^{21,22}. G-type antiferromagnetism (AFM) is formed at a Néel temperature of $T_N = 5.5 \text{ K}$ with $7\mu_B$ on each Eu^{2+} site^{23,24}. Moreover, multiferroic properties due to strong spin-lattice coupling has been shown by first-principle calculations²⁵ and via strain-effect²². Recent experiments reveal evidence of the existence of topology-related phenomena including skyrmion-like Hall effect²⁶ and Weyl nodes²³ in doped ETO. It is reported that a highly mobile and spin-polarized 2DEG could be realized within the heterostructure of EuO/KTO ²⁷ based on which thermal spin injection was realized¹³ and superconductivity was observed^{15,16,28}. Similarly, EuO/TaO_2 interface can be also realized within the ETO/KTO heterostructure, which may as well host 2DEG with strong SOC and exotic magnetic and topological properties.

Here we report electric transport measurements on both LTO/KTO and ETO/KTO heterostructures. LTO and ETO were deposited onto substrates of KTO respectively by the molecular beam epitaxy (MBE) method. We observed Kondo effects for the temperature dependence of resistivity and corrections to magnetoresistance due to superposition of weak anti-localization (WAL) and weak localization (WL) for both samples. The extracted magnetic coherence length l_φ and spin-orbit coupling length l_{SO} are smaller for ETO/KTO in comparison with LTO/KTO, suggesting the different origin of SOC. Since Rashba effect should be similar for both heterostructures as both 2DEGs reside in KTO near the interface, the distinguished strong WAL for ETO/KTO should originate from the proximity effect of the topological band structure of ETO, which is supported by its anomalous Hall effect. Our results provide an effective way for tuning and engineering topological properties of band structure into KTO-based heterostructure which can be extended to other interfacial electronic systems.

Results

Temperature-dependence of resistivity. Samples were prepared by molecular beam epitaxy (MBE) method and high crystalline quality was achieved (see Fig. 1 and *Methods*). Both samples have shown the typical densities of 2DEG carriers in KTO (Supplementary Information Fig. 2) from oxygen vacancies formed during high temperature annealing, and electronic reconstruction due to the polar nature of KTO¹⁹. Although polar catastrophe has been proposed to be another origin of 2DEGs, experimental evidence remains missing.

Figure 1(d & e) exhibits the temperature dependence of resistivity below 20 K. Both types of samples exhibit metal-insulator transitions. For LTO/KTO, the transition takes place at 10.2 K, below which it firstly exhibits an upturn with approximate $\ln(T)$ dependence, and starts to saturate from 300 mK down to 30 mK. Such a temperature dependence is characteristic of the Kondo effect originating from the interplay of itinerant electrons and magnetic impurities, and the

saturation implies screening of magnetic impurities by bound electrons via spin-exchange interactions. The temperature dependence can be fitted by the empirical relation^{29,30}

$$R(T) = R_0 + R_K(T) = R_0 + R_K(0) \left[\left(\frac{T}{T_K} \right)^2 \left(2^{\frac{1}{s}} - 1 \right) + 1 \right]^{-s} \quad \# (1)$$

where R_0 is temperature independent resistance including residual resistance due to sample disorder and extra resistance associated with weak localization (WL) or weak antilocalization (WAL), T_K the Kondo temperature, and s a parameter related with spin. Here we fix $s = 0.22$ for spin $S = 1/2$ ³⁰ and get a satisfactory fitting with $T_K = 1.21$ K.

In comparison, the ETO/KTO sample exhibits the metal-insulator transition at 12.1 K and a well-fitted Kondo behavior below 1.50 K with $s = 0.22$ and $T_K = 1.49$ K. There are two wiggle points at 3.85 K and 1.50 K, which lead to the resistance below 1.50 K shifting downwards. The shift may be ascribed to the suppression of electron back-scattering associated with the emergence of topology to conducting band, which will be discussed later.

Localization effects of magnetoresistance. Magnetoresistance (MR) has been measured for both samples at multiple temperatures (see Fig. 2). MR of the LTO/KTO sample demonstrates a sharp feature within the narrow range of ± 0.05 T at 0.25 K. With an increasing magnetic field, resistivity firstly increases and starts to decrease for $|B| > 0.015$ T. Such a feature becomes less obvious as the temperature is raised and vanishes at around 3 K. Besides the MR near the zero field, an extra dip of resistance is observed around zero field at 4 K with a half-width of 0.05 T. The dip develops into a plateau with larger width and smoother edge at lower temperatures, and the edge eventually merged with the universal background. One possible explanation of this is that part of the sample becomes superconducting similar to EuO/KTO and LAO/KTO¹⁵. However, this scenario cannot be confirmed without further investigation by other techniques such as scanning tunneling spectroscopy (STS). A similar feature in MR is observed for the ETO/KTO sample in a similar temperature range but with much larger magnitude and in a much wider magnetic field range of ± 0.5 T. However, no feature of an additional plateau similar to that for LTO/KTO is observed.

The superposition of positive and negative MR suggests the coexistence of both weak localization (WL) and weak anti-localization (WAL)³¹. In the diffusive transport process, maintenance of phase coherence causes phase interference, therefore leading to an increase in resistivity, while the existence of SOC causes destructive interference and leads to a decrease in resistivity. Correction of WL and WAL to conductivity can be described by the theory of Iordanskii, Lyanda-Geller, and Pikus (ILP)³²

$$\Delta\sigma(B) = -\frac{e^2}{\pi h} \left[\frac{1}{2} \psi \left(\frac{1}{2} + \frac{B_\varphi}{B} \right) - \frac{1}{2} \ln \left(\frac{B_\varphi}{B} \right) - \psi \left(\frac{1}{2} + \frac{B_\varphi + B_{SO}}{B} \right) + \ln \left(\frac{B_\varphi + B_{SO}}{B} \right) - \frac{1}{2} \psi \left(\frac{1}{2} + \frac{B_\varphi + 2B_{SO}}{B} \right) + \frac{1}{2} \ln \left(\frac{B_\varphi + 2B_{SO}}{B} \right) \right]$$

where $B_\varphi = \frac{\hbar}{4el_\varphi^2}$ is the dephasing magnetic field determined by the phase coherence length l_φ , $B_{SO} = \frac{\hbar}{4el_{SO}^2}$ is the spin-orbit scattering field determined by the spin-orbit scattering length l_{SO} , and $\psi(x)$ is the digamma function.

We find that Eq. (2) can fit the feature of MR very well for both samples as shown in Fig. 3 and Fig. 4, and the extracted values of l_φ and l_{SO} are plotted in Fig. 3 (e,f) and Fig. 4 (e,f), respectively. On one hand, these two characteristic lengths of both samples share some properties in common: l_φ scales with $T^{-1/2}$, and the exponent of -1/2 indicates that the transport is two-dimensional; l_{SO} does not observe to be obviously temperature-dependent. On the other hand, characteristic lengths of LTO/KTO are significantly larger than those of ETO/KTO: for LTO/KTO, $l_\varphi = 200\bar{2}32$ nm and $l_{SO} \approx 190$ nm, while for ETO/KTO, $l_\varphi = 130\bar{1}80$ nm and $l_{SO} \approx 50$ nm. In comparison, mean free path (l_{mfp}) for both samples are around 20 nm (see Supplementary Fig. 2), smaller than l_φ and l_{SO} . The ILP theory is derived for the diffusive regime, i.e. $B < \frac{\hbar}{2el_{mfp}^2}$. The value of l_{mfp} constrain the validity of the ILP model within the magnetic field of ± 0.8 T, in consistence with valid range of the fitting to the ETO/KTO sample. However, the ILP model fits the MR of the LTO/KTO sample in a much smaller range, probably because spin canting and rotation of TiO6 tetrahedral caused by external field are more obvious due to the smaller magnetic moment of Ti³⁺^{14,24}.

The extracted characteristic lengths l_φ and l_{so} are plotted in (e) as functions of $T^{-\frac{1}{2}}$. The green dashed line in panel (e) is a linear fit, demonstrating that $l_\varphi \propto T^{-\frac{1}{2}}$.

The fact that l_φ being larger than l_{SO} guarantees the phase coherence during the spin-orbit scattering process, leading to the obvious positive MR (or negative magnetoconductance) associated with the WAL effect. We note that the magnitude of conductance change $\Delta\sigma$ for the LTO/KTO sample is about one order of magnitude smaller than that for the ETO/KTO sample ($\bar{0}.01e^2/h$ vs. $\bar{0}.2e^2/h$). This is because the difference between l_φ and l_{SO} is much smaller ($\frac{l_\varphi}{l_{SO}} \approx 1.1$ for LTO/KTO vs. 3.0 for ETO/KTO), and the effects of WL partially cancel that of WAL on conductance. However, both characteristic lengths for the LTO/KTO sample are significantly larger than those for the ETO/KTO sample, suggesting either much more scattering sites existing in the ETO/KTO sample to destroy phase coherence and to cause spin flips or the transport process is governed by different nature of conducting band. The former possibility is unlikely thanks to the similar quality of crystalline and interfaces for both samples, while the latter is highly possible due to the much larger magnetic moment on Eu²⁺ sites and the possible topological band of ETO²³.

Anomalous Hall effect. Since itinerant electrons reside in KTO for both cases, the magnitude of Rashba coupling should be similar and cannot account for the difference of WAL effect between the two samples. To clarify the origin of the stronger scattering in the ETO/KTO sample, we performed Hall measurements for both samples (Supplementary Information Fig. 1). In spite of the quasi-linear dependence of ρ_{xy} on the magnetic field, a weak anomalous Hall effect can

still be observed. Figure 5 shows the anomalous hall resistance ρ_{AHE} extracted by subtracting ρ_{xy} by an ordinary Hall term $\rho_H \propto \alpha B$, where α is a coefficient determined by a linear fit of ρ_{xy} between 3 T and 4 T. ρ_{AHE} for LTO/KTO is negative (namely $\rho_{AHE} < 0$ for $B > 0$) and temperature-independent below 5 K. In stark contrast, ρ_{AHE} for ETO/KTO is positive and exhibits a strong temperature dependence until it vanishes above 5 K. Furthermore, its magnitude – at 0.5 K for example – is about 10 times larger than that of LTO/KTO.

Discussions

In Fig. 5(b), we find that ρ_{AHE} at 2 K saturates at about 2 T. This is consistent with the magnetization of ETO^{23,33}. Furthermore, the onset temperature of ρ_{AHE} is also close to the Neel temperature of ETO ($T_N = 5.5$ K). Both evidences support that the AHE is highly related with the proximity of ETO. It has been pointed out that non-trivial Berry curvature can be induced and controlled in ETO by applying external magnetic field²³. Induced Zeeman splitting in the process of canting magnetic moments causes type II Weyl nodes and topologically changes the band structure of ETO. The high similarity between the measured ρ_{AHE} and magnetization in ETO suggests that electrons at the ETO/KTO interface are strongly influenced by the topological band structure of ETO. The emergence of ρ_{AHE} – becoming obvious below about 5 K – also coincides with the wiggle points appearing in the $\rho - T$ curve in Fig. 1(e). The emergence of wiggle point could be due to the suppression of electron back-scattering associated with spin-orbit locking. In contrast, ρ_{AHE} for the LTO/KTO sample, being temperature independent and much weaker, should solely stem from the topology induced by Rashba-type SOC in KTO. The Rashba effect is weakly temperature dependent below 5 K because of its higher spin-orbit split band^{34,35}, leading to the temperature independence of ρ_{AHE} .

In summary, we have studied the transport properties of 2DEG residing near the interfaces of both LaTiO₃/KTaO₃ and EuTiO₃/KTaO₃ heterostructures, and observed superposition of weak localization and weak anti-localization effects. The extracted phase coherence length $l_\varphi \propto T^{-1/2}$ and l_{SO} is temperature independent, confirming the existence of spin-orbit coupling in both heterostructures, while characteristic lengths of ETO/KTO are much smaller, implying the coupling mechanism is different. By analyzing the anomalous Hall effect, we found that AHE for ETO/KTO features with a positive sign, strong temperature dependence, and large magnitude, different from the LTO/KTO sample. We deduce that such a difference, together with the localization effects, stems from the strong topological band induced by the ETO film.

Methods

Sample preparation and structural characterization. All films were grown on insulating KTO (001) substrates (MTI). The lattice constant of KTO is 3.99 Å, larger than ETO (3.905 Å) and LTO (3.97 Å), which results in the tensile strain in all epitaxial films.

The samples were grown in an oxide molecular beam epitaxial (MBE) system (Veeco GenXplor) with a base pressure $< 5 \times 10^{-10}$ torr. The flux ratio between Eu, La, and Ti was calibrated by quartz crystal microbalance, and the film growth process and the number of layers were monitored and determined by in-situ reflection high-energy electron diffraction.

At the temperature of 700°C, KTO substrate was annealed for 30 min without oxygen to degas. After that, ETO film was grown on the substrate by co-deposition in a partial pressure of molecular oxygen pressure of $4-5 \times 10^{-8}$ Torr. LTO film was also grown by co-deposition in a partial pressure of molecular oxygen pressure of $3-4 \times 10^{-8}$ Torr. After the film growth, all samples were capped with 5 nm of amorphous Ge at room temperature to prevent sample deterioration during the ex-situ measurements. Bare KTO substrate, after the same annealing process and 5 nm of amorphous Ge capping, shows clear insulating behavior. Same growth methods generate insulating/stoichiometric ETO and LTO films on another insulating substrate²⁴.

After the growth and capping, the films were characterized by X-ray diffraction (XRD, Bruker) in the $2\theta-\omega$ mode for the structural information using Cu K α 1 radiation.

Electrical transport measurement and data analyses. Electric transport measurements were performed on a dilution refrigerator (Oxford Triton500). Van der Pauw (VdP) method was used for the transport measurements, with both LTO/KTO and ETO/KTO samples in a square shape with dimensions of 5×5 mm² and electric contacts made to four corners by indium-soldering. The Standard lock-in technique was used with a frequency of 17 Hz and a current of 1 μ A. Longitudinal resistance R_{xx} was measured by running current through two contacts on the same edge, and Hall resistance R_{xy} by running current through two contacts on diagonal. Due to the finite contact size and non-ideal symmetry, anti-symmetrization was performed to extract R_{xy} . Pictures were taken for the samples after the contacts were made. Transport processes were then simulated by finite element modeling (FEM) using COMSOL. The simulations were run with ρ_{xx} and ρ_{xy} as input parameters to match the experimental results.

Declarations

Acknowledgements

The work at IOP-CAS was supported by National Key R&D Program of China (2021YFA1401900 & Grant No. 2018YFA0305604), National Natural Science Foundation of China (NSFC) (No. 11874403), Key Research Program of Frontier Sciences, CAS, (Grant No. ZDBS-LY-SLH0010), and Beijing Natural Science Foundation (Grant No. JQ21002). The work at UBC was supported by Natural Sciences and Engineering Research Council (NSERC) of Canada and Canada Foundation for Innovation (CFI).

Author contributions

Z.G.C. and K.Z. conceived and designed the experiments, Y.Z., H.S., H.W. and B.A.D. fabricated and measured the devices. Z.G.C. wrote the manuscript with comments from all other authors.

Additional Information

Competing financial interests: the Authors declare no Competing Financial or Non-Financial Interests.

References

- Ohtomo, A. & Hwang, H. Y. A high-mobility electron gas at the LaAlO₃/SrTiO₃ heterointerface. *Nature* **427**, 423–426 (2004).
- Reyren, N. *et al.* Superconducting Interfaces Between Insulating Oxides. *Science* **317**, 1196–1199 (2007).
- Brinkman, A. *et al.* Magnetic effects at the interface between non-magnetic oxides. *Nat. Mater.* **6**, 493–496 (2007).
- Li, L., Richter, C., Mannhart, J. & Ashoori, R. C. Coexistence of magnetic order and two-dimensional superconductivity at LaAlO₃/SrTiO₃ interfaces. *Nat. Phys.* **7**, 762–766 (2011).
- Caviglia, A. D. *et al.* Tunable Rashba Spin-Orbit Interaction at Oxide Interfaces. *Phys. Rev. Lett.* **104**, 126803 (2010).
- Caviglia, A. D. *et al.* Two-dimensional quantum oscillations of the conductance at LaAlO₃/SrTiO₃ interfaces. *Phys. Rev. Lett.* **105**, 236802 (2010).
- Caviglia, A. D. *et al.* Electric field control of the LaAlO₃/SrTiO₃ interface ground state. *Nature* **456**, 624–627 (2008).
- Herranz, G. *et al.* Engineering two-dimensional superconductivity and Rashba spin–orbit coupling in LaAlO₃/SrTiO₃ quantum wells by selective orbital occupancy. *Nat. Commun.* **6**, 6028 (2015).
- Thompson, J. R., Boatner, L. A. & Thomson, J. O. Very low-temperature search for superconductivity in semiconducting KTaO₃. *J. Low Temp. Phys.* **47**, 467–475 (1982).
- Wemple, S. H. Some Transport Properties of Oxygen-Deficient Single-Crystal Potassium Tantalate (KTaO₃). *Phys. Rev.* **137**, A1575–A1582 (1965).
- Mattheiss, L. F. Energy Bands for KNiF₃, SrTiO₃, KMoO₃, and KTaO₃. *Phys. Rev. B* **6**, 4718–4740 (1972).
- Zhang, H. *et al.* Highly Mobile Two-Dimensional Electron Gases with a Strong Gating Effect at the Amorphous LaAlO₃/KTaO₃ Interface. *ACS Appl. Mater. Interfaces* **9**, 36456–36461 (2017).
- Zhang, H. *et al.* Thermal Spin Injection and Inverse Edelstein Effect of the Two-Dimensional Electron Gas at EuO/KTaO₃ Interfaces. *Nano Lett.* **19**, 1605–1612 (2019).
- Zou, K. *et al.* LaTiO₃/KTaO₃ interfaces: A new two-dimensional electron gas system. *APL Mater.* **3**, 036104 (2015).
- Liu, C. *et al.* Two-dimensional superconductivity and anisotropic transport at KTaO₃ (111) interfaces. *Science (80-.)*. **371**, 716–721 (2021).
- Ma, Y. *et al.* Superconductor-Metal Quantum Transition at the EuO/KTaO₃ Interface*. *Chinese Phys. Lett.* **37**, 117401 (2020).
- Chen, Z. *et al.* Electric field control of superconductivity at the LaAlO₃/KTaO₃(111) interface. *Science (80-.)*. **372**, 721–724 (2021).
- Chen, Z. *et al.* Two-Dimensional Superconductivity at the LaAlO₃/KTaO₃(110) Heterointerface. *Phys. Rev. Lett.* **126**, 026802 (2021).
- Gupta, A. *et al.* KTaO₃ – The New Kid on the Spintronics Block. *Adv. Mater.* 2106481 (2021) doi:10.1002/adma.202106481.
- Yuan, N. F. Q. & Fu, L. Topological metals and finite-momentum superconductors. *Proc. Natl. Acad. Sci.* **118**, e2019063118 (2021).
- Maruhashi, K. *et al.* Anisotropic Quantum Transport through a Single Spin Channel in the Magnetic Semiconductor EuTiO₃. *Adv. Mater.* **32**, 1–10 (2020).
- Lee, J. H. *et al.* A strong ferroelectric ferromagnet created by means of spin–lattice coupling. *Nature* **466**, 954–958 (2010).
- Takahashi, K. S. *et al.* Anomalous Hall effect derived from multiple Weyl nodes in high-mobility EuTiO₃ films. *Sci. Adv.* **4**, 1–9 (2018).
- Shin, H. *et al.* Controlling the electrical and magnetic ground states by doping in the complete phase diagram of titanate Eu_{1-x}LaxTiO₃ thin films. *Phys. Rev. B* **101**, 214105 (2020).
- Fennie, C. J. & Rabe, K. M. Magnetic and Electric Phase Control in Epitaxial EuTiO₃ from First Principles. *Phys. Rev. Lett.* **97**, 267602 (2006).
- Ahadi, K., Galletti, L. & Stemmer, S. Evidence of a topological Hall effect in Eu_{1-x}SmxTiO₃. *Appl. Phys. Lett.* **111**, 172403 (2017).
- Zhang, H. *et al.* High-Mobility Spin-Polarized Two-Dimensional Electron Gases at EuO/KTaO₃ Interfaces. *Phys. Rev. Lett.* **121**, 116803 (2018).
- Liu, C. *et al.* Tunable superconductivity at the oxide-insulator/KTaO₃ interface and its origin. (2022).
- Lee, M., Williams, J. R., Zhang, S., Frisbie, C. D. & Goldhaber-Gordon, D. Electrolyte Gate-Controlled Kondo Effect in SrTiO₃. *Phys. Rev. Lett.* **107**, 256601 (2011).

30. Costi, T. A. *et al.* Kondo Decoherence: Finding the Right Spin Model for Iron Impurities in Gold and Silver. *Phys. Rev. Lett.* **102**, 056802 (2009).
31. Albright, S. D., Zou, K., Walker, F. J. & Ahn, C. H. Weak antilocalization in topological crystalline insulator SnTe films deposited using amorphous seeding on SrTiO₃. *APL Mater.* **9**, 111106 (2021).
32. Iordanskii, S. V., Lyanda-Geller, Y. B. & Pikus, G. E. Weak localization in quantum wells with spin-orbit interaction. *JETP Lett.* **60**, 206 (1994).
33. Takahashi, K. S., Onoda, M., Kawasaki, M., Nagaosa, N. & Tokura, Y. Control of the Anomalous Hall Effect by Doping in Eu_{1-x}La_xTiO₃ Thin Films. *Phys. Rev. Lett.* **103**, 057204 (2009).
34. King, P. D. C. *et al.* Subband Structure of a Two-Dimensional Electron Gas Formed at the Polar Surface of the Strong Spin-Orbit Perovskite KTaO₃. **117602**, 1–5 (2012).
35. Nakamura, H. & Kimura, T. Electric field tuning of spin-orbit coupling in KTaO₃ field-effect transistors. *Phys. Rev. B* **80**, 121308 (2009).

Figures

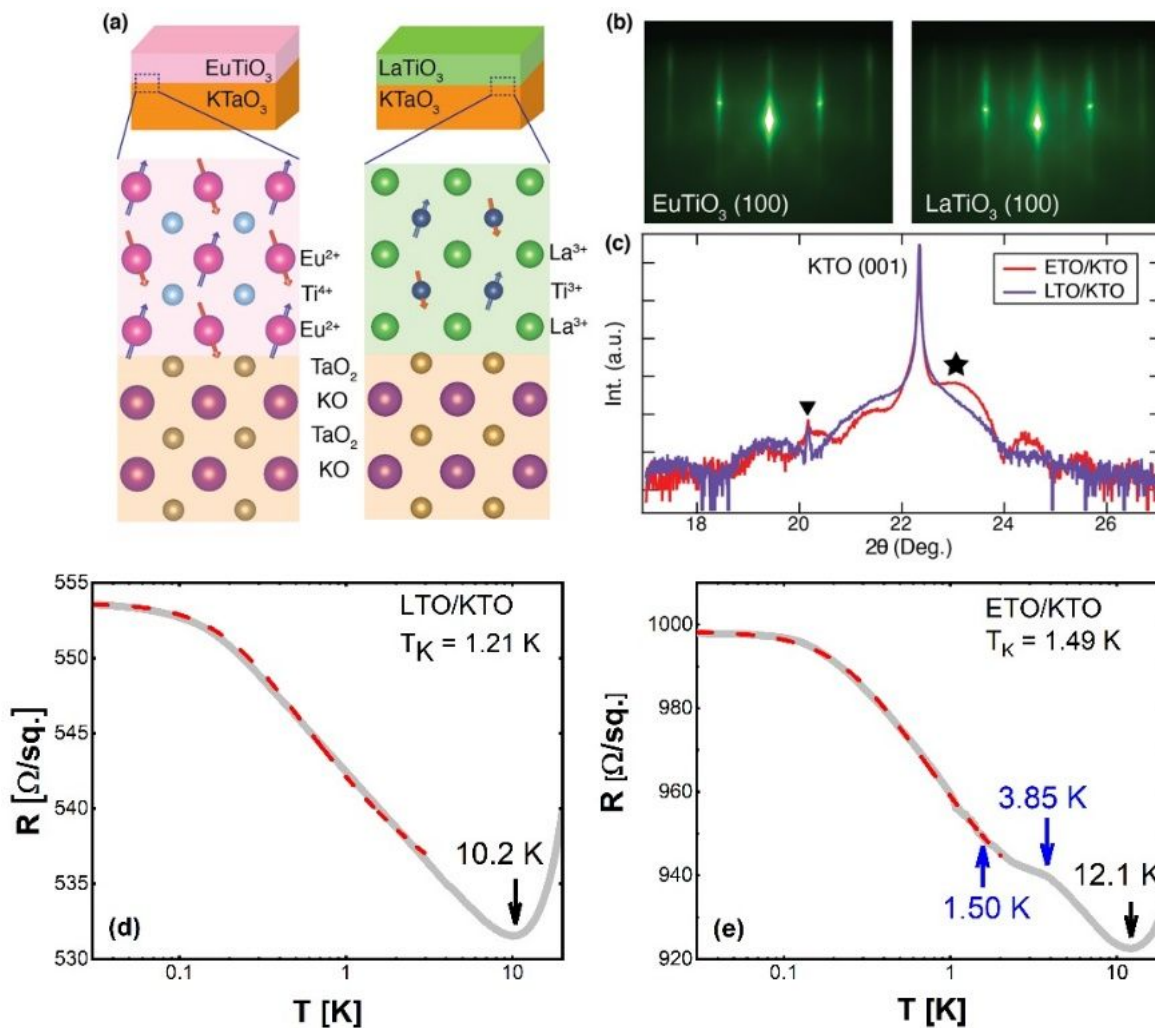


Figure 1

(a) schematic picture of EuTiO₃/KTaO₃ (left) and LaTiO₃/KTaO₃ (right) heterostructures and their atomic and antiferromagnetic spin structures (below). The size of spins on the Eu²⁺ and Ti³⁺ indicates the relative magnitude of magnetic moments ($7\mu_B/\text{Eu}$ and $7\mu_B/\text{Ti}$). (b) in-situ reflection high-energy electron diffraction (RHEED) intensity picture of EuTiO₃ and LaTiO₃ after 10 u.c. growth. (c) XRD scan of 20 u.c. EuTiO₃/KTaO₃ (red) and 10 u.c. LaTiO₃/KTaO₃ (purple). The symbol \star and \blacktriangledown indicate the (001) peak of EuTiO₃ and carbon paste defect, respectively. Temperature dependence of resistivity is plotted in (d) for the sample of LTO/KTO and in (e) for the sample of ETO/KTO.

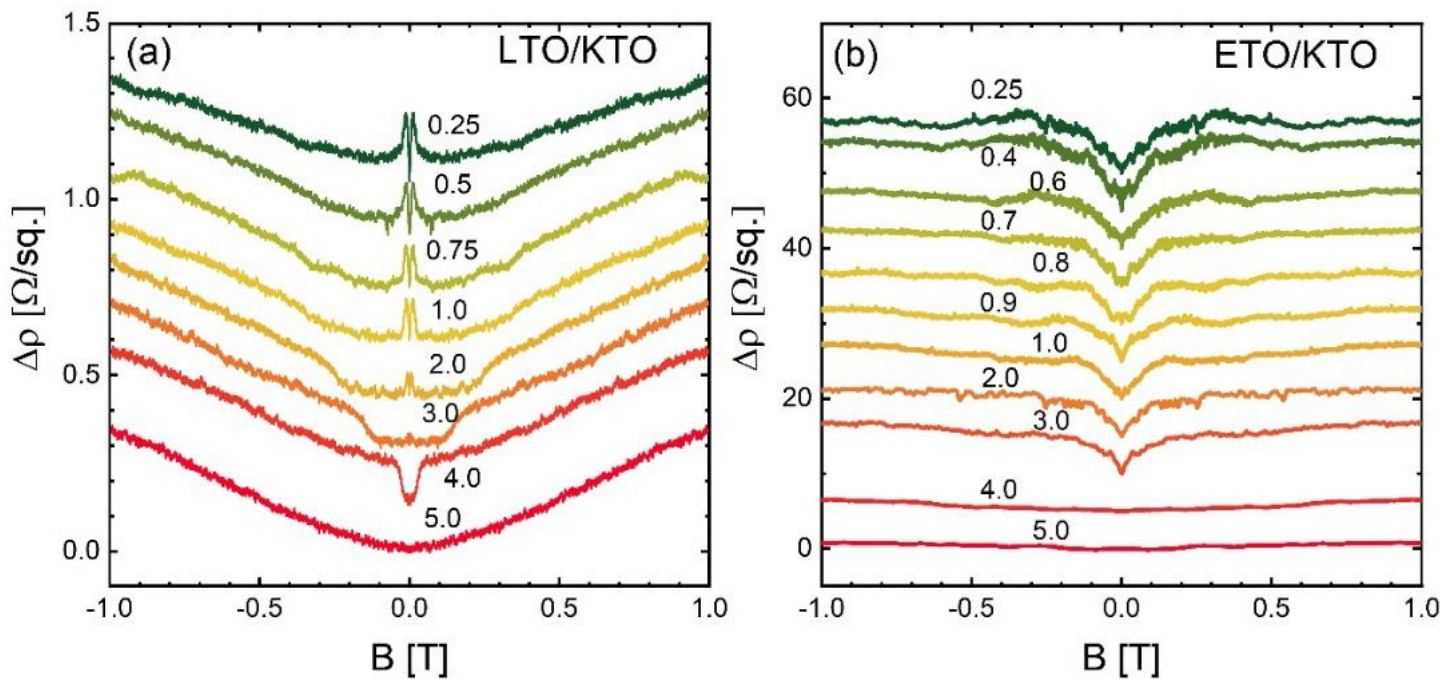


Figure 2

Magnetoresistance of both samples. $\Delta\rho=\rho(B)-\rho(0)$. Curves are vertically shifted, and temperatures for each MR curve are labeled.

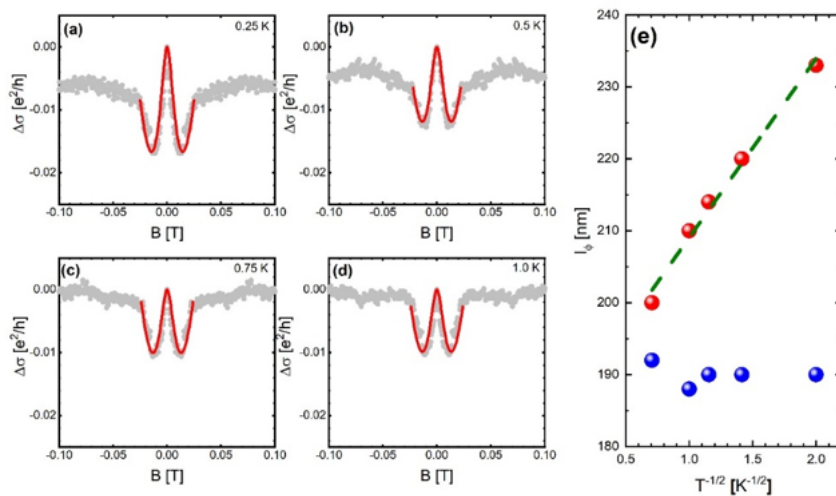


Figure 3 (a-d) Conductance of the LTO/KTO sample at various temperatures. Grey dots are experimental data and red solid lines are fitting curves based on HLN theory. The extracted characteristic lengths l_ϕ and l_{s0} are plotted in (e) as functions of $T^{-\frac{1}{2}}$. The green dashed line in panel (e) is a linear fit, demonstrating that $l_\phi \propto T^{-\frac{1}{2}}$.

Figure 3

See image above for figure legend

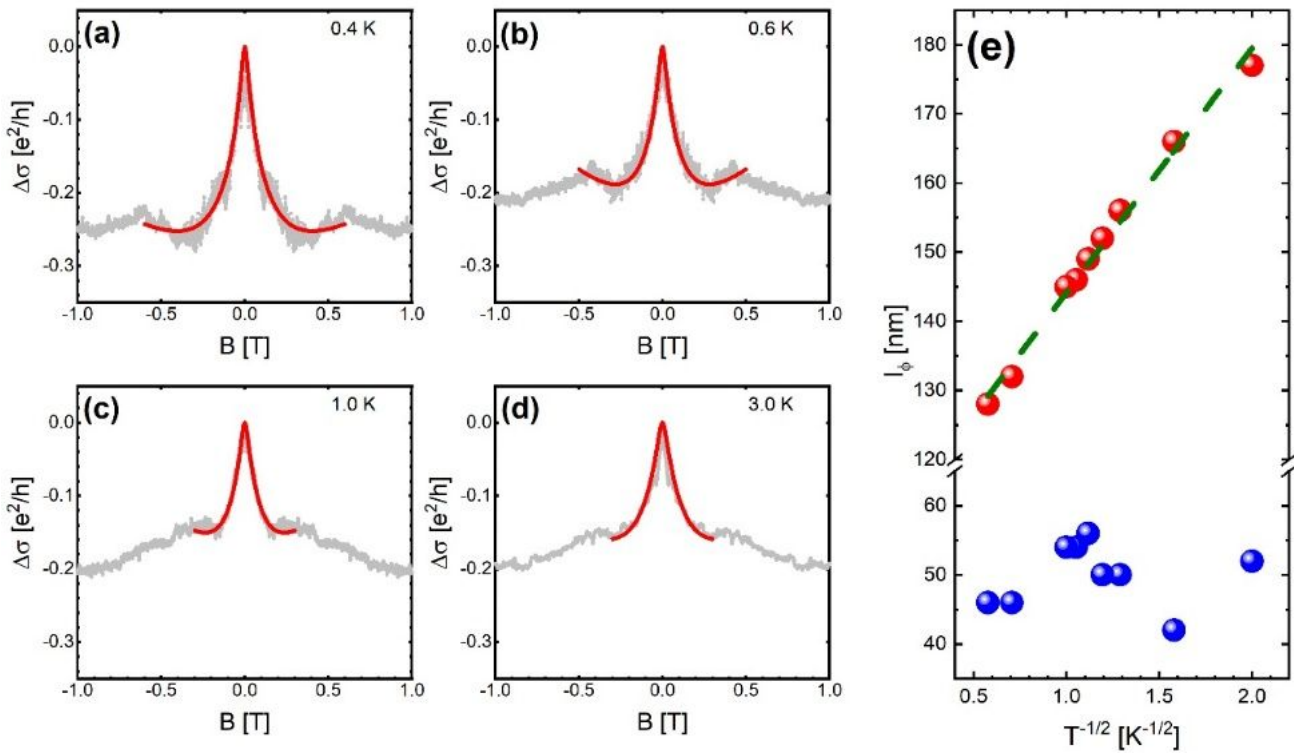


Figure 4

(a-d) Conductance of the ETO/KTO sample at various temperatures. Grey dots are experimental data and red solid lines are fitting curve based on HLN theory.

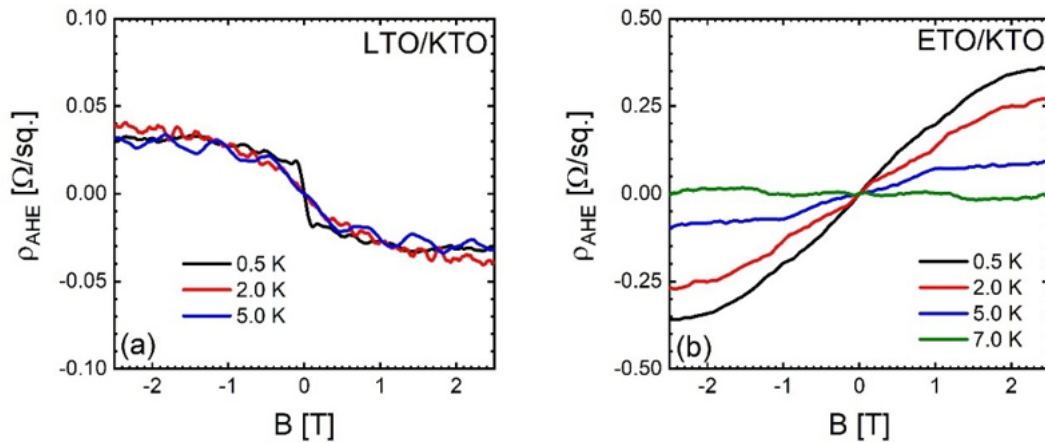


Figure 5 Anomalous Hall resistivity versus magnetic field for the sample of LTO/KTO (a) and ETO/KTO (b). $\rho_{AHE} = \rho_{xy} - \rho_H = \rho_{xy} - \alpha B$, where α is a fitting parameter.

Figure 5

See image above for figure legend

Supplementary Files

This is a list of supplementary files associated with this preprint. Click to download.

- [KTOSI20220421final.docx](#)